Expanding the understanding of squeeze flow with pressure mapping and application for concentrated suspensions

Franco A. Grandes[1,2] · Fábio A. Cardoso[1,2] · Rafael G. Pileggi[1,2]

Abstract

Squeeze flow has been proven as an interesting technique for the rheological evaluation of many classes of materials, being relatable to common compressive phenomena from various processing and application procedures. Despite the simplicity of the experimental setup needed to run it, the results from the test are rather complex, involving multiple variables and factors that are not fully clarified by the bulk stress response. One additional piece of information that can be valuable is the pressure distribution over the sample area, since it is related to key aspects of the flow. The addition of a pressure mapping system to the traditional setup of the test has been recently proposed as a way to enrich the information obtained, in a method deemed pressure mapped squeeze flow (PMSF). This paper presents the evolution and state of the art of this technique, and analyzes a plastic clay with two different water contents in three displacement rates to demonstrate the potential and possibilities that PMSF offers. The experimental setup is presented in detail, along with the calibration procedure and data treatment suggested, as well as multiple types of analyses including bulk stress curves, raw pressure distribution plots, measured contact area, evolution of the mean profile, comparison to theoretical models supported by error analysis, and investigation of variation over the area. With the procedure established and presented in this work, it should be possible to apply PMSF as a valuable technique throughout the materials science and engineering community.

Keywords Squeeze flow · Pressure mapping · Suspensions · Ceramics · Phase separation

Introduction

Proper rheological evaluation is a key aspect for many types of materials regarding processing, quality control, and performance. For most engineering materials, the rheological response depends not only on their characteristics, but also on the stresses and strains applied, being affected by geometrical restrictions during flow as well. The same material may present diverse behaviors under different sets of stimuli; thus, parameters from rheological tests should be taken as an estimate of the behavior tied to the characteristics of the measurement conducted (Coussot 2005), and the behavior described should be considered as an answer to a given set of conditions (Min et al. 1994). Among many

traditional rheometric techniques, the squeeze flow test is a versatile method based on compressive rheometry that has been employed for a wide array of fluids, suspensions, and soft solids (Engmann et al. 2005), being relatable to the conditions found in different types of practical situations, such as chewing and swallowing for foods (Campanella and Peleg 1987; Steffe 1996; Stading 2021); molding processes of polymers (Kotsikos et al. 1996; Törnqvist et al. 2000); and pumping, injection, spraying, spreading, finishing, and extrusion of cementitious materials (Grandes et al. 2018, 2021).

Despite having relatively easy application, the response during squeeze flow is complex, and there is more information to be obtained from the test than the basic bulk normal force vs. displacement result. The nature of the flow is transient due to the geometric modification (Engmann et al. 2005), and different types of flow may occur during the test, depending on the material characteristics, geometry, and boundary conditions, including the ratio between sample radius and height, plate roughness, and lubrication (Steffe 1996; Meeten 2004). These multiple factors together

✉ Rafael G. Pileggi
  rafael.pileggi@lme.pcc.usp.br

1 National Institute On Advanced Eco-Efficient Cement-Based Technologies, São Paulo, Brazil

2 Department of Construction Engineering, Escola Politécnica, University of São Paulo, São Paulo 05508-070, Brazil

influence the type of flow, which may also change during the test and even be different for specific parts of the sample. Due to these complexities, attempts to create models rely on hypotheses, approximations, and considerations that can be hard to validate or confirm for each case (Lipscomb and Denn 1984; Muravleva 2015). One element that is directly related to the type of flow — being also affected by the same factors — is the pressure distribution along the interfaces between sample and plates. Due to this correlation, the pressure distribution can help to further describe and identify flow characteristics and rheological behavior for a given moment of squeeze flow (Adams et al. 1991; Muravleva 2015), elucidating the analysis and the influence of multiple variables involved in the test.

For traditional simple shear rheometric techniques with fixed geometry, wall slip, fracture, and other problems of homogeneity may happen and hinder the validity of the test. The compressive nature of squeeze flow not only lessens the occurrence of these issues (Rabideau et al. 2009), but also allows the test to still produce valid results and return valuable information even in these situations (Engmann et al. 2005), making it a powerful tool to explore and evaluate these phenomena and transitions between flow types. This is even more relevant for granular materials and pastes, since under confined flow and gap reduction situations they may present multiple behaviors and other intricate fluid dynamics (Coussot 2005). Flow-induced microstructural changes and phase separation are also common for these materials (Collomb et al. 2004; Roussel and Lanos 2004; Cardoso et al. 2009), making each situation unique regarding the overall resulting behavior and enhancing the transient nature of the flow.

Throughout the decades, many researchers and papers highlighted that further evidence regarding the nature of the flow, interfacial conditions, and other phenomena can be beneficial for the interpretation of the results (Chatraei et al. 1981; Adams et al. 1991; Kotsikos et al. 1996; Estellé et al. 2006). Additional instrumentation of squeeze flow can provide new evidence of these phenomena (Adams et al. 1991), and some experimental solutions proposed were even able to identify the occurrence of phase separation in model suspensions (Nikkhoo et al. 2013). Pioneer publications with a pressure mapping system for the evaluation of mortars (multiphasic materials with wide granular extension) demonstrated the potential of the technique to analyze complex dynamics and changes on a microstructural level (Grandes et al. 2018, 2021), but also highlighted the necessity of a work with simpler materials focused on describing the method and its own intricacies.

This paper employs dynamic pressure mapping in combination with squeeze flow to evaluate clay suspensions, in order to demonstrate the viable uses and present the state of the art of the method with detailed experimental procedure, data treatment route, and possible types of analyses. It also compares results with findings and conclusions from previous works.

Assessing the pressure profile during squeeze flow — literature review

Considering the relevance of that information for the analyses, researchers have employed different types of complementary devices to evaluate the pressure distribution during squeeze flow tests. Localized pressure transducers in perfect plastic materials have been used for the determination of interfacial conditions during the tests (Adams et al. 1991), to ascertain changes in the pressure profile under different conditions (Adams et al. 1993), and even to support the validation of a finite elements analysis (Adams et al. 1997).

A similar setup with 3 pressure transducers incorporated into the plates allowed for a rough estimate of the pressure profile during the squeeze flow of polymeric compounds, leading to inferences regarding the boundary conditions and more information about the behavior of the material during the compression molding process (Kotsikos and Gibson 1998; Kotsikos et al. 1999). The evolution of the pressure distribution obtained indicated a mixed flow closer to biaxial extension than to shear flow, clearer for higher displacements and pressure levels (Fig. 1a). Regarding resolution and homogeneity, assessing only a few points of the sample limits the detailing of the measurement; thus, this setup requires the assumption that the pressure distribution and flow type are homogeneous all over the sample area.

A pressure-sensitive film that registers the maximum pressure reached, positioned along a radial axis of the samples, was employed for the analysis of simplified suspensions of glass spheres in silicon oil (Nikkhoo et al. 2013). The pressure profiles obtained (Fig. 1b) demonstrated that, up to a certain solid content, the suspensions behaved as Newtonian fluids under shear flow, but above a critical solid
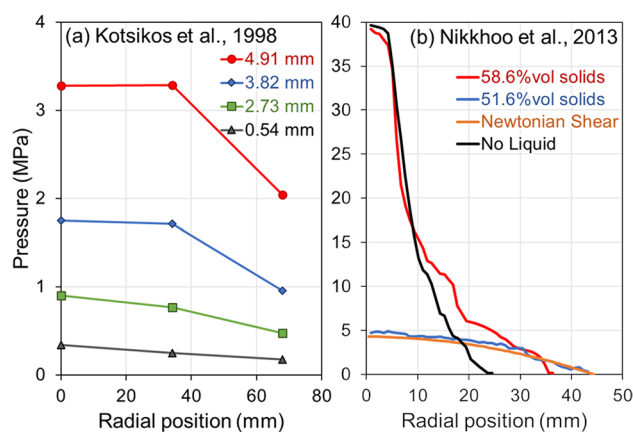
Fig. 1 Example results from the literature of pressure distribution during squeeze flow of **a** sheet molding compound tested at 0.1 mm/s in 4 selected displacements (initial sample height of 6 mm) (Kotsikos and Gibson 1998) and **b** suspensions of glass spheres in silicon oil with 3 different solid contents, no liquid phase, and prediction for a Newtonian fluid under shear flow (Nikkhoo et al. 2013)

content, pressure concentration peaks were observed in the central region. This led to pressure profiles similar to the one from the compression of spheres with no liquid, indicating a predominantly frictional behavior. Further evidence from measurements of the solid content in multiple regions of the samples proved that the peaks were caused by liquid phase radial migration (Nikkhoo et al. 2014).
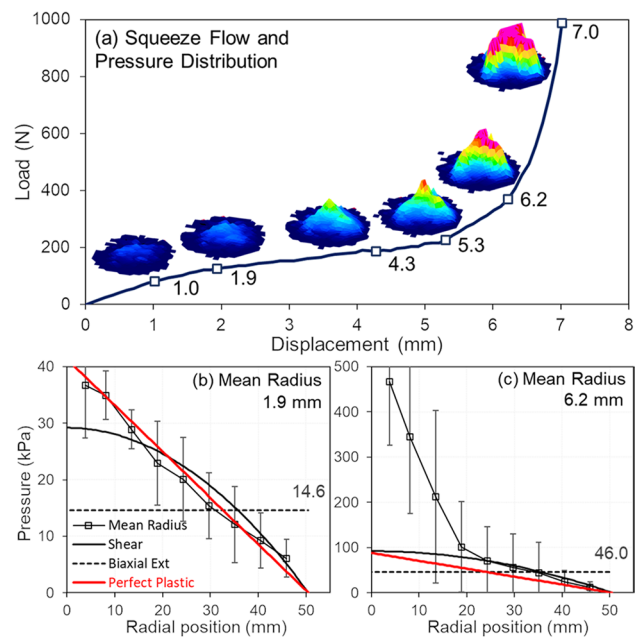
While localized transducers can assess the evolution of the pressure in specific points of the sample, heterogeneities along the sample area — especially relevant for suspensions — and other phenomena may go unnoticed by the technique. Pressure-sensitive films and similar technologies may offer a wider covered area than transducers; however, not collecting real-time data and registering only the maximum pressure make it difficult to analyze the evolution of the pressure distribution during the test. A more sophisticated technique that covers these limitations is dynamic interfacial pressure mapping, which was employed in association with squeeze flow pioneeringly to evaluate Newtonian fluids, clays, and foods (Yates 2003). The addition of pressure mapping to the test enabled real-time measurements of the evolution of the pressure distribution all over the sample area in a considerable resolution, as shown by the selected example results displayed in Fig. 2. Parabolic profiles indicate shear flow predominance for the materials and conditions of the test presented in that
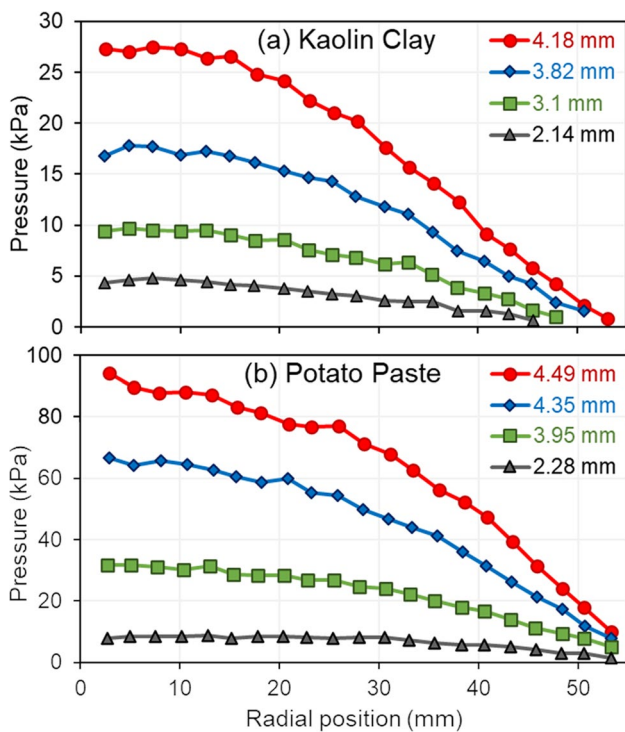
work. The results were also compared with predictions from a power law model to estimate rheological parameters.

Inspired by the novel information that the combination of techniques could generate, the pressure mapped squeeze flow method was developed for the evaluation of cement-based mortars, initially in a constant area squeeze flow configuration (Grandes et al. 2018). Cement mortars have varying compositions, with multiple phases, wide granular extension, up to 30% of entrained air content, and possibly admixtures with numerous effects (Cardoso et al. 2014). The intrinsic heterogeneities of the material make the flow under the geometric restrictions and changes from the squeeze test even more complex. The new evidence from pressure mapped squeeze flow (PMSF) provided brand new insight regarding phase separation and related phenomena, with visualization of the concentration peaks caused by particle jamming (supported by quantification of the liquid phase migration) and comparison to the predictions from theoretical models (Fig. 3). The frictional behavior led to exponential pressure distribution in the regions affected by separation, while other areas showed profiles indicating a more viscous flow — either close to Newtonian shear flow or to plastic deformation. The work also demonstrated other effects caused by intrinsic heterogeneities present during the squeeze flow of some mortars (such as multiple eccentric pressure concentration peaks) and an analysis of stress relaxation after the end of the

Fig. 2 Example results for selected displacements of pressure mapped squeeze flow of **a** kaolin clay (initial height 5 mm; displacement rate 0.1 mm/s) and **b** potato paste (initial height 5 mm; displacement rate 0.083 mm/s), adapted from Yates (2003)


Fig. 3 Example of PMSF in the constant area configuration from (Grandes et al. 2018): **a** squeeze flow results with 3D plots of the pressure distribution; and mean profile analysis including comparison with models for two displacements, **b** 1.9 mm and **c** 6.2 mm

test, all supported and made possible by the combination of techniques.

More recently, another work (Grandes et al. 2023) employed the same test setup to analyze a variety of factory-produced mortars. PMSF was able to demonstrate particularities of the flow of different products available in the building materials market. The results corroborated previous findings regarding materials with high susceptibility to phase separation (Grandes et al. 2018) while also showing mortars with more homogeneous behavior, including an analysis of variation to distinguish between them. The paper also compared results from PMSF and other rheometric tests (rotational and flow table), showing that different sets of stimuli can lead to different rheological responses from the same material and demonstrating the importance of combining techniques for the analysis of complex flows.

Squeeze flow is also commonly employed using the constant volume configuration, in which the whole sample is in between the plates for the duration of the test and the velocity field depends only on boundary conditions from the interfaces (Denn and Marrucci 1999). Figure 4 illustrates the experimental setup for constant volume squeeze flow of a cement mortar with the incorporation of the pressure mapping device (Grandes et al. 2021).

The first work with constant volume PMSF on mortars (Grandes et al. 2021) provided a new way to analyze changes in the sample area during the tests (Fig. 5), which can be an obstacle in the analysis when the incompressibility hypothesis is not accurate. The method demonstrated not only an influence of loss of entrained air (with air bubbles, common in mortars, collapsing during the test) and its relation to the intensity of phase separation, but also how the differential flow affects the sample through variations in the measured area. With the new information provided by PMSF, it was possible to identify transitions into more frictional flows
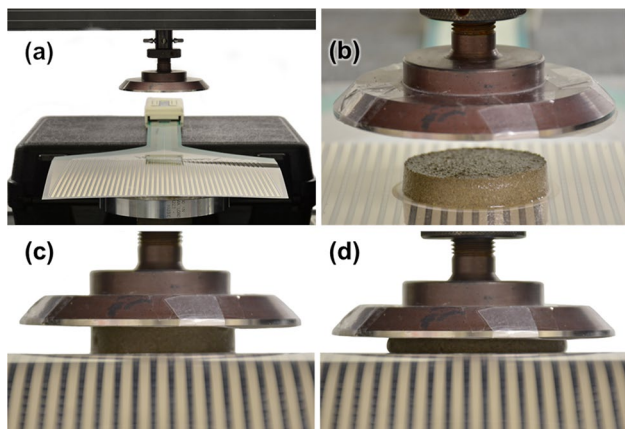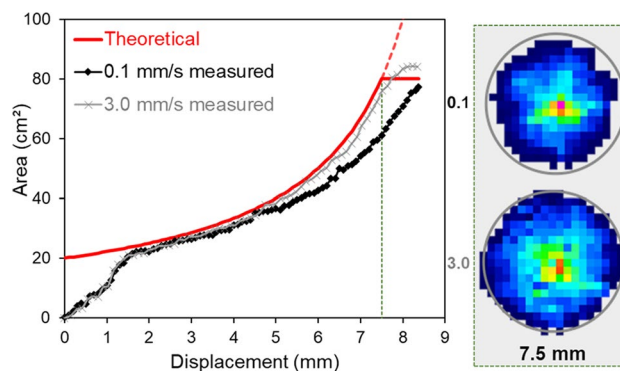
Fig. 5 Measured area during PMSF with constant volume configuration for a factory-produced mortar in two displacement rates and comparison to theoretical area from constant volume hypothesis (Grandes et al. 2021)

starting from the central area of the sample, and the behavior and microstructural changes were then further explained and illustrated using interparticle separation concepts.

Squeeze flow involves the particularity of possibly inducing phase separation and other phenomena due to the geometric changes caused by its compressive nature. This makes the test a powerful rheometric tool to evaluate these intricate aspects of the flow that can also take place during the practical application of materials and possibly lead to negative influence on their performance. However, more details and information about the flow are required to analyze such a complex response, reason why the instrumentation of the test with pressure mapping becomes so relevant. With this, the sensitivity of the test to all the factors involved becomes even more evident due to the amount of information gathered. Knowing how to handle possible limitations, the experimental specifics, and the ways to analyze the raw information obtained is crucial for the employment of this method. The present work is a contribution to disseminate PMSF as a useful tool for the characterization of fluids, granular suspensions, and soft solids under squeeze flow, as it explains in detail the full experimental procedure, calibration, data treatment, and multiple ways to analyze the data in the current state of the art of the technique.

Experimental

Materials

This work analyzes suspensions of a commercial plastic clay designed for lathe, modeling, and molding that produces white ceramic products after sintering at 1300 °C. The suspensions were prepared with two different water contents (42.5% and 49% liquid volume fraction (LVF), or 27.9% and 36.3% water content as commonly expressed for the Atterberg limits). The Atterberg

Fig. 4 Pressure mapped squeeze flow setup: **a** sensor and universal testing machine, **b** sample positioning, **c** beginning of the test, **d** undergoing test — adapted from Grandes et al. (2021)

method (Andrade et al. 2011) measured plastic limit (PL) of 20.1% water content (ABNT NBR 7180) and liquid limit (LL) of 47.4% (ABNT NBR 6459), resulting in a plasticity index (PI) of 27.3%. Figure 6a situates the contents employed between the Atterberg limits in a linear representation, for both types of the water fraction metrics presented. Equation 1 presents the formula for liquid volume fraction, with V_w being the volume of water, V_s being the volume of solids, and V_T being the total volume, and Eq. 2 shows the calculation for water content, with M_w being the mass of water and M_s being the mass of solids.

$$LVF(\%vol) = \frac{V_w}{V_T} = \frac{V_w}{V_w + V_s} \tag{1}$$

$$WC(\%w) = \frac{M_w}{M_s} \tag{2}$$

Figure 6b shows the position of the clay powder in the plasticity chart, commonly employed for the classification of soils. The material lands in the "low-plasticity clay" area, but close to the border for high-plasticity clays. This clay has similar classification as other materials previously analyzed that were deemed adequate for lathe (or throwing wheel) molding (Ino et al. 2020).

The choice of material aimed to provide an analysis of a more homogeneous flow in relation to what was seen in previous works with cement mortars. The particle size distribution (Helos, Sympatec) is presented in Fig. 7a. The X-ray diffractometry (Philips X'Pert Pro PW 3040) performed detected kaolinite, muscovite, quartz, and gibbsite phases (Fig. 7b), and the X-ray fluorescence (S8 Tiger, Bruker) is also presented in Fig. 7c. The dry powder had a density of 2.65 g/cm^3.
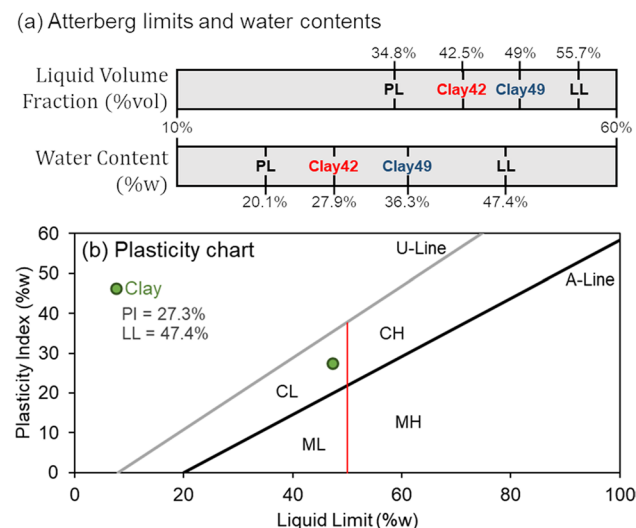

Fig. 6 **a** Representation of the Atterberg limits and water contents employed, both in liquid volume fraction and water content. **b** Localization of the clay in the plasticity chart for classification of soils
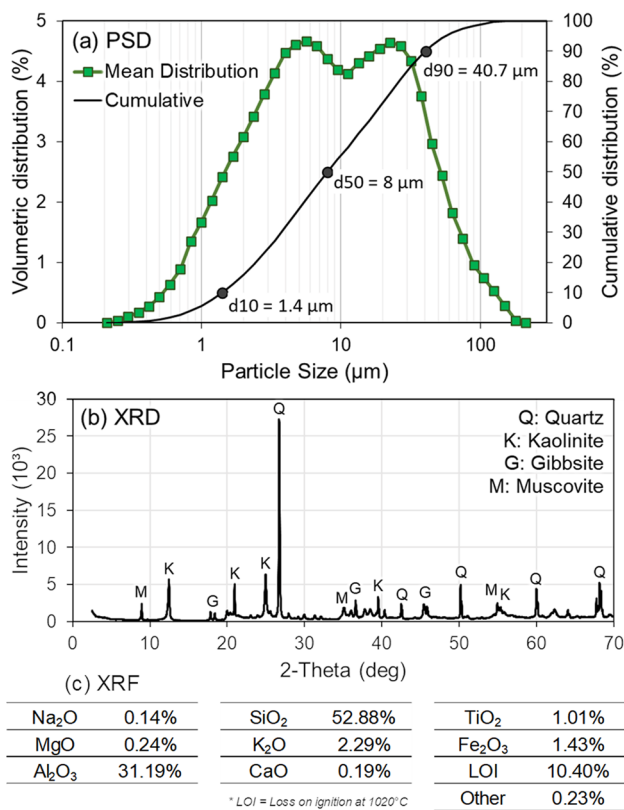
Fig. 7 Characterization of the plastic clay: **a** particle size distribution, **b** X-ray diffractometry, and **c** X-ray fluorescence

Sample preparation

To obtain the plastic clay suspensions, deionized water (for each of the two contents) was added to the dry clay powder, and then the mixture was left in an airtight container for 24 h for homogenization and water distribution. For the tests, cylindrical samples were molded initially with 50 mm of diameter (which is smaller than the upper plate and thus constitutes constant volume configuration) and 11 mm of height. The sample was compacted with a manual roller, the height was adjusted with a template of wood fillets (Fig. 8b), and the diameter was set by a stainless-steel cutter (Fig. 8c). Although the air content was not measured, it is believed that after this compacting procedure the entrained air in the resulting samples was not significant. For the tests in this work, the sample preparation procedure was performed over a cellulose acetate sheet (common transparency sheet for projectors) with 100 μm of thickness. This step was performed to facilitate the transfer to the PMSF setup (further explained in the "Pressure mapped squeeze flow (PMSF)" section) and to avoid water loss by substrate absorption during sample molding. A new sample from the same batch was prepared for testing at each displacement rate.
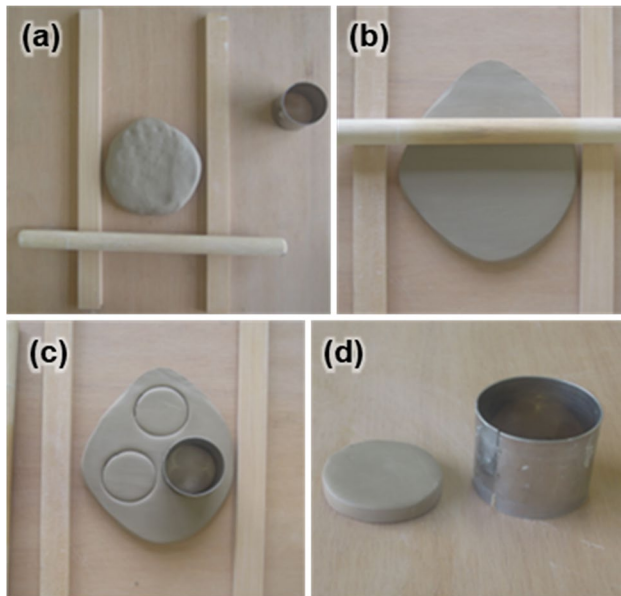
Fig. 8 Sample preparation: **a** clay and tools employed, **b** compaction of the sample mass using a manual roller and wood fillets to adjust the height, **c** cutting of the sample with a stainless-steel cylinder, **d** final sample ready for the test (adapted from Ino et al. 2020)

Pressure mapped squeeze flow (PMSF)

PMSF tests were performed in a laboratory with controlled temperature (23 °C) and humidity, using a two-column universal testing machine (INSTRON 5569) with a 1-kN load cell, controlled displacement in 3 different rates (0.1, 1.0, and 5.0 mm/s), and 7 mm of maximum displacement (from an initial sample height of 11 mm). The maximum load of the system is 50 kN and the maximum load set for the tests was 1 kN. The frame compliance for that level of load as indicated by the manufacturer (Reference Manual M10-14190-EN) is 0.006 mm, lower than the overall accuracy of the measurement (0.02 mm) and even lower than the minimum displacement step employed (0.1 mm); thus, it was considered that no significant deflection of the crosshead occurred. An upper plate with 101 mm diameter was fixed to the load cell at the crosshead, and the bottom plate was mounted over the fixed compression base of the equipment. Because the upper plate employed has approximately double the diameter of the sample, constant volume configuration is ensured until the maximum displacement. Plates were made of steel with smooth surface, but polymeric films were employed on the interfaces.

The evolution of the pressure distribution during the tests was assessed by a dynamic pressure mapping system (I-Scan, Tekscan Inc.) with a sensor (FlexiForce 5210N, Fig. 9) that consists of two thin, flexible polyester sheets with electrically conductive electrodes: one sheet forms a row pattern, while the other forms a column pattern. The intersections of these rows and columns create a mesh of piezoresistive sensing elements (*sensels*)
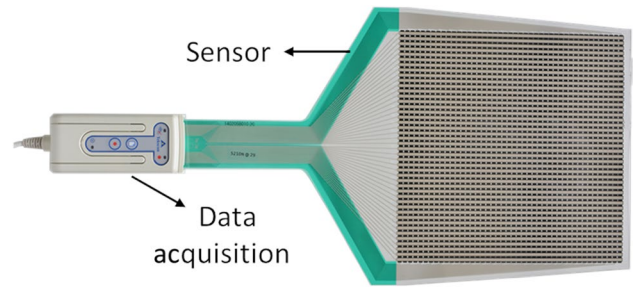
Fig. 9 Pressure mapping sensor (FlexiForce 5210N, Tekscan) and data acquisition unit employed

with a density distribution of 3.4 sensel/cm^2 over a square area with sides of 238 mm. Electrical resistance of the sensels varies inversely with applied load and the software of the I-Scan system processes that signal, allowing adjustments in sensor sensitivity and in data sampling. The maximum total pressure of the sensor used is 83 kPa (or 12 psi) and the sensitivity of the sensor was kept constant at a value of 31 (on a scale from 1 to 40). Data acquisition rate was defined to match the ones used in the universal testing machine (10 data/mm of displacement). The mapping system linearizes sensor output into digital counts, or "raw" values, on a scale from 0 to 255. The raw values can be compared if tests are performed with the same sensor and sensitivity (as in the "Bulk squeeze flow stress curves and raw pressure distribution" section). To transform raw values into real engineering units, sensor data must be calibrated, and the calibration process is further explained in the "Sensor data calibration and treatment" section.

The setup of the experiment is the same illustrated in Fig. 4 (except that in those images the sample is from a cement-based mortar). The pressure sensor was positioned on the bottom plate and connected to the I-Scan software (Fig. 4a). The samples of clay were cast, immediately before testing, over a cellulose acetate sheet, and then the sheet and sample were placed over the sensor (Fig. 4b). This polymeric sheet was used to facilitate molding and positioning as well as to avoid damage of the sensor, especially at the final stages of the test, when particles can be compressed against the sensor. Preliminary tests demonstrated that the presence of this sheet does not affect the results. The upper plate (which was also covered by a plastic film to set a similar interfacial condition as the bottom plate) was lowered until it slightly touched the sample (Fig. 4c), and the experiment started; Fig. 4d illustrates the condition during the test.

Results and discussion

Bulk squeeze flow stress curves and raw pressure distribution

The squeeze flow stress vs. displacement curves for the 6 tests performed are presented in Fig. 10, as well as 3D plots of the
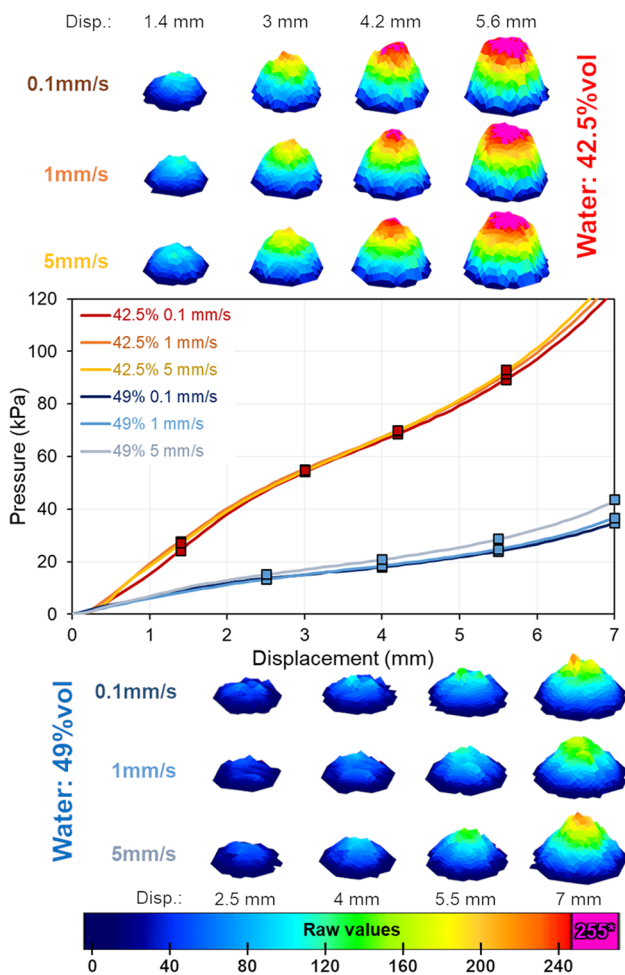
Fig. 10 Squeeze flow stress vs. displacement and 3D plots of pressure distribution at specific displacements

pressure distribution in a raw color scale for four selected displacements of each test. For each set with the same water content, the tests in different displacement rates show very similar bulk squeeze stress behavior, with slightly higher pressures for the higher displacement rates. This suggests no significant influence of liquid phase migration (Cardoso et al. 2009; Grandes et al. 2018) (further discussed in the "Evolution of the pressure distribution" section). The clay with lower water content had higher pressure, but still a relatively homogeneous growth of both the bulk stress and the pressure distribution profiles. Towards the end of these tests, some saturation of the sensor occurred, as evidenced by the pink regions at the center of the 3D plots for 5.6 mm of displacement.

Even with uncalibrated pressure distribution plots, it is already possible to see that the behavior is quite different than what was observed for cement mortars in the same test setup (Grandes et al. 2021). The profiles are parabolic shaped and regular throughout the tests, without clear concentration peaks, indicating a much more homogeneous flow than what
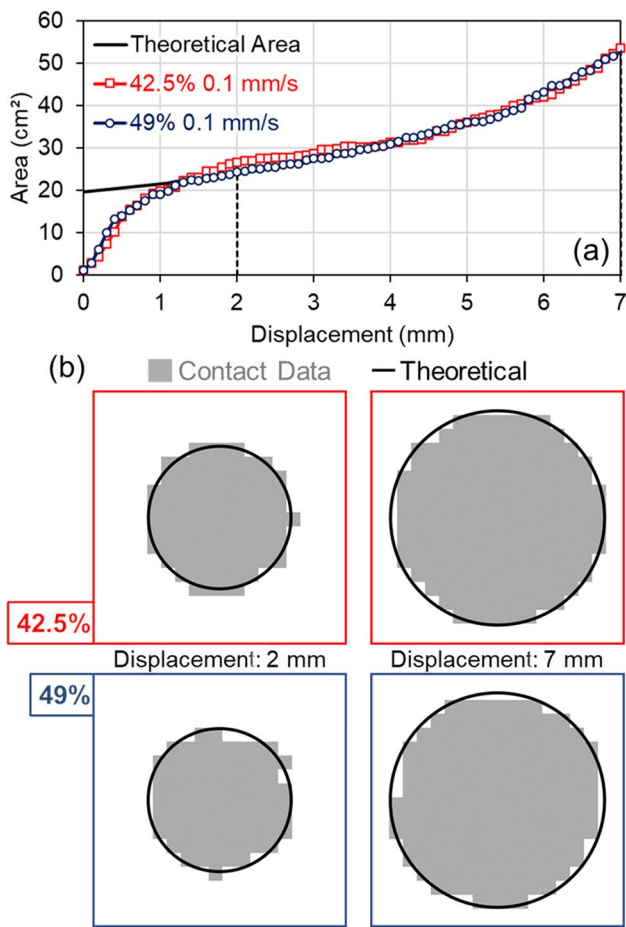
was previously seen. Besides the technological relevance of plastic clays, the choice of material for this work was made aiming to demonstrate the technique and its potential in a different type of flow, without the interference of intrinsic heterogeneities and other effects caused by the wider granular extension of mortars. The relatively bigger particles commonly found in cement mortars create a more granular response specially when phase separation takes place, leading to a predominantly frictional Coloumb-like behavior that takes over the bulk force in the form of strain hardening (Grandes et al. 2018, 2021) which does not happen in the more homogeneous flow observed during the tests presented in this paper.

Sensor contact area vs. theoretical area

In the constant volume configuration of squeeze flow, the area of the sample being compressed changes during the test. The sample area can be estimated by the change in sample height using an incompressibility hypothesis; however, that might not represent well the reality during the test for many materials. Some fluids may include compressible fractions, and other materials (often the case for mortars) may include a considerable amount of entrained air or even the presence of molding flaws. The pressure mapping system employed can provide additional information of the contact area during the tests, and with that also a better understanding of the phenomena involved (Grandes et al. 2021).

Figure 11a presents the comparison between the theoretical area calculated from the incompressibility hypothesis and the contact area measured by the sensor for the tests at 0.1 mm/s for clay samples with both water contents. After an initial accommodation period up to 1 mm of displacement (when the pressure is too close to the lower measuring limit of the sensor), the measured values of sample area were very close to the incompressibility estimation for the duration of both tests depicted in the graphic. That behavior differs from what has been previously seen for cement mortars (Grandes et al. 2021), which showed a lower measured area in relation to the theoretical area for higher displacements, due to both loss of entrained air and intense phase separation effects. Figure 11a shows a behavior once again compatible with homogeneous flow with low or no phase separation.

The curve for the test with the clay with 42.5% of water shows a slightly higher area than the theoretical curve from around 1.5 to 3.5 mm. The difference, however, is not significant and can be explained by the resolution of the sensor grid, since even if only part of a sensing element is activated by pressure the whole *sensel* square area (29.16 mm^2) is counted. Figure 11b shows the representation of the contact area data from the sensor for two moments of the tests (2 mm and 7 mm of displacement), as well as the circular representation of the theoretical area calculated for each of those moments. This representation helps to show the

Fig. 11 Comparison between theoretical area considering constant sample volume and contact area measured by the pressure sensor for tests with both water contents at 0.1 mm/s: (**a**) evolution of the area values throughout the tests; (**b**) visual representation of active elements from the sensor and theoretical area for two selected displacements of each test

and better representation of the results, initially explored in a more recent work (Grandes et al. 2023) and described in further detail for the first time here.

Up to ten data points distributed over the displacement range before significant sensor saturation took place were selected for each test, associating the raw values measured by the pressure sensor with the corresponding load value given by the universal testing machine at the same moment. The sensor digital output is then converted to engineering units according to the correlation obtained by the comparison. Figure 12 presents the comparison between the final calibrated I-Scan force and the universal testing machine load curves for the six tests analyzed, and the calibration points employed.

Since the pressure range is relatively wide, sensor saturation occurred towards the end of the tests with lower water content, and some information is lost in the saturated regions (initiated in the central region of the samples, where the pressure levels are higher). For this reason, the data for the last part of these tests is not suitable for the calibration process, and consequently load and calibrated force curves start to gradually diverge (Fig. 12a,b,c). That occurs because the pressure on saturated regions is higher than the value measured by the sensor (maximum detectable pressure for the employed setup). To avoid this, a different sensor or sensitivity setup could be used; however, that would come at the cost of losing precision and resolution for the moments of the test and regions of the sample with lower pressure results. For the clay with 49% of water content on the other hand, no significant saturation occurred until the end of the tests for all three displacements (Fig. 12d,e,f), and the sensor force curves remained close to the load curves for the whole range of those tests.

The calibrated sensor data of interest consisted of matrixes of 20×20 in size, with one set of values for each

effect of the resolution of the sensor rendering a pixelated version of a circle, with each square pixel being one *sensel*. The activated areas from the sensor remain relatively close to the theoretical area even at 2 mm of displacement for the clay with 42.5% of water, the moment that the graphic from Fig. 11a shows relatively higher measured area.

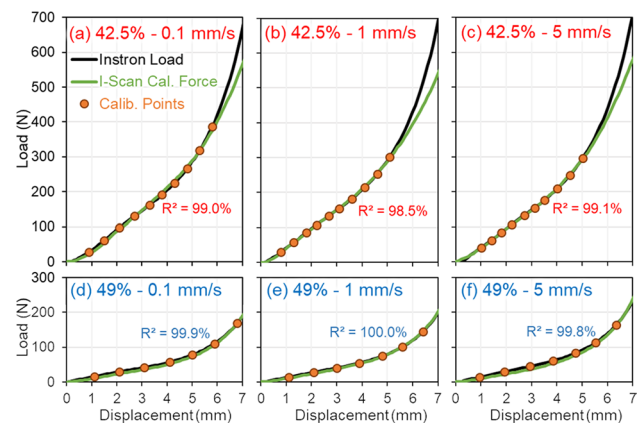## Sensor data calibration and treatment

To enable quantitative analyses with the pressure distribution results, sensor data must be transformed into real engineering units; thus, a calibration process is required. For that, it is possible to use the actual squeeze flow load values from each test since the universal testing machine provides precise and reliable information. The calibration procedure employed in this work is an improved version from the first works with this method (Grandes et al. 2018, 2021) to ensure more precision
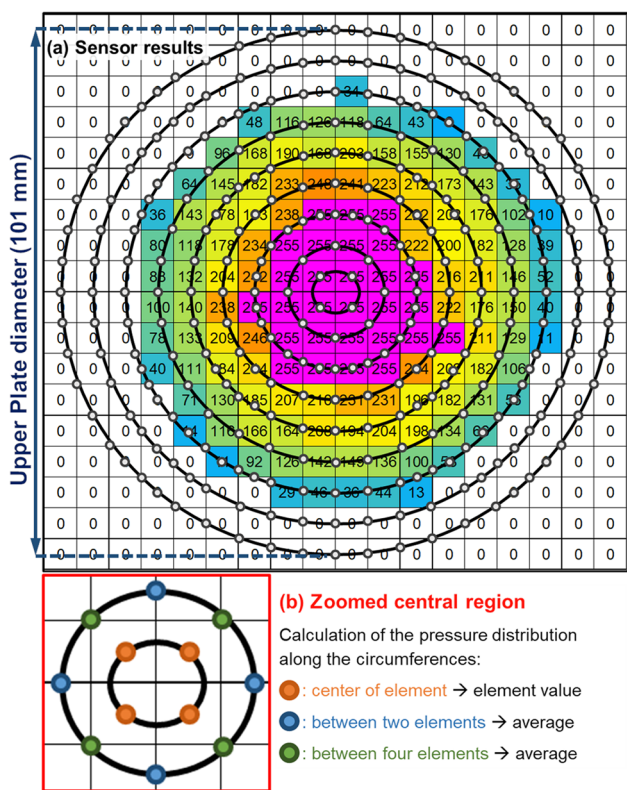

Fig. 12 Calibration of the pressure mapping system results: comparison between measured load from the testing machine and pressure sensor calibrated force for the tests performed with the clay with (**a**)-(**c**) 42.5% and (**d**)-(**f**) 49% of water content

0.1 mm of displacement of each test. The main strategy adopted to treat this amount of data and allow for a better analysis of the pressure distributions is deemed mean profile (previously "mean radius" (Grandes et al. 2021)). The pressure along nine concentric circumferences within the sensor area was determined using data sets composed of the output from the sensing elements (either the value itself or interpolated data from 2 to 4 elements) according to the representation shown in Fig. 13, which overlaps raw sensor data from one moment of the test at 1 mm/s of the clay with 42.5% water as an example. The values obtained were used to determine the mean pressure and standard deviation for each circumference (from "R1" closest to the center with 3.8 mm of radius, to "R9" closest to the border with 45.9 mm). This allows for a quick visualization of the pressure distribution, creating a representation of the distribution over the whole contact area between the sample and the sensor in a single graphic.

To avoid visual bias hindering the analysis of calibrated results, data points highly influenced by sensor saturation were omitted from graphics. When more than 20% of the

points along a given circumference were saturated, the resulting data point was not included in the graphic representation. An example of a data set with elevated saturation on the three inner circumferences is shown on Fig. 14 with and without the saturated points to demonstrate the difference. Even though the saturation hinders part of the data set, a valid analysis of the pressure distribution information from the rest of the sample area can still be performed excluding the affected points.

Evolution of the pressure distribution

Using the calibrated results and mean profile data treatment described in the "Sensor data calibration and treatment" section, the evolution of the pressure distribution for each test is shown in Fig. 15, with the mean pressure profile for four selected displacements (organized by tests in a to f) and coefficient of variation (CV) for each data point (shown in bar graphics in a-CV to f-CV). It is important to highlight that since the tests were performed under the constant volume squeeze flow configuration, the area of the sample and the radial position of the border changes, and the pressure variation is affected by border effects (also because the lower pressure in those regions is closer to the measurement limit of the sensor). For that reason, the bars representing CV tend to show higher values close to the border, but for metrology reasons rather than an actual response from the material.

Even though overall the results of the tests in the three different displacement rates for each water content seem to be generally similar, a closer look with this representation shows further details and small differences that could not be detected by the bulk squeeze flow curves in the "Bulk squeeze flow stress curves and raw pressure distribution" section. Regarding the variation parameter, the test at 5 mm/s with the 42.5% clay (Fig. 15c-CV) seems to have consistently lower coefficient of variation than the lower rates (Fig. 15a-CV and Fig. 15b-CV), which is an indicator
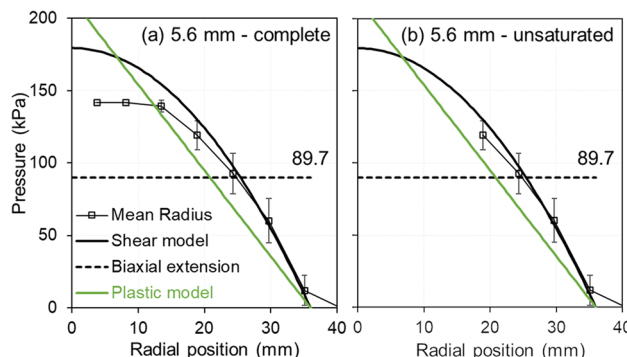

Fig. 13 Mean profile analysis: pressure calculation in each circumference. Example shown for 5.6 mm of displacement of the 1 mm/s test using the plastic clay with 42.5% of water: (**a**) position of the circumferences and pressure determination points (grey points) over sensor grid with results in raw scale; (**b**) zoomed central region detailing the three types of points and how the pressure is determined depending on position relative to the element

Fig. 14 Pressure distribution results representation with **a** all data points and **b** excluding saturated results at 5.6 mm of displacements for the plastic clay with 42.5% of water tested at 1 mm/s
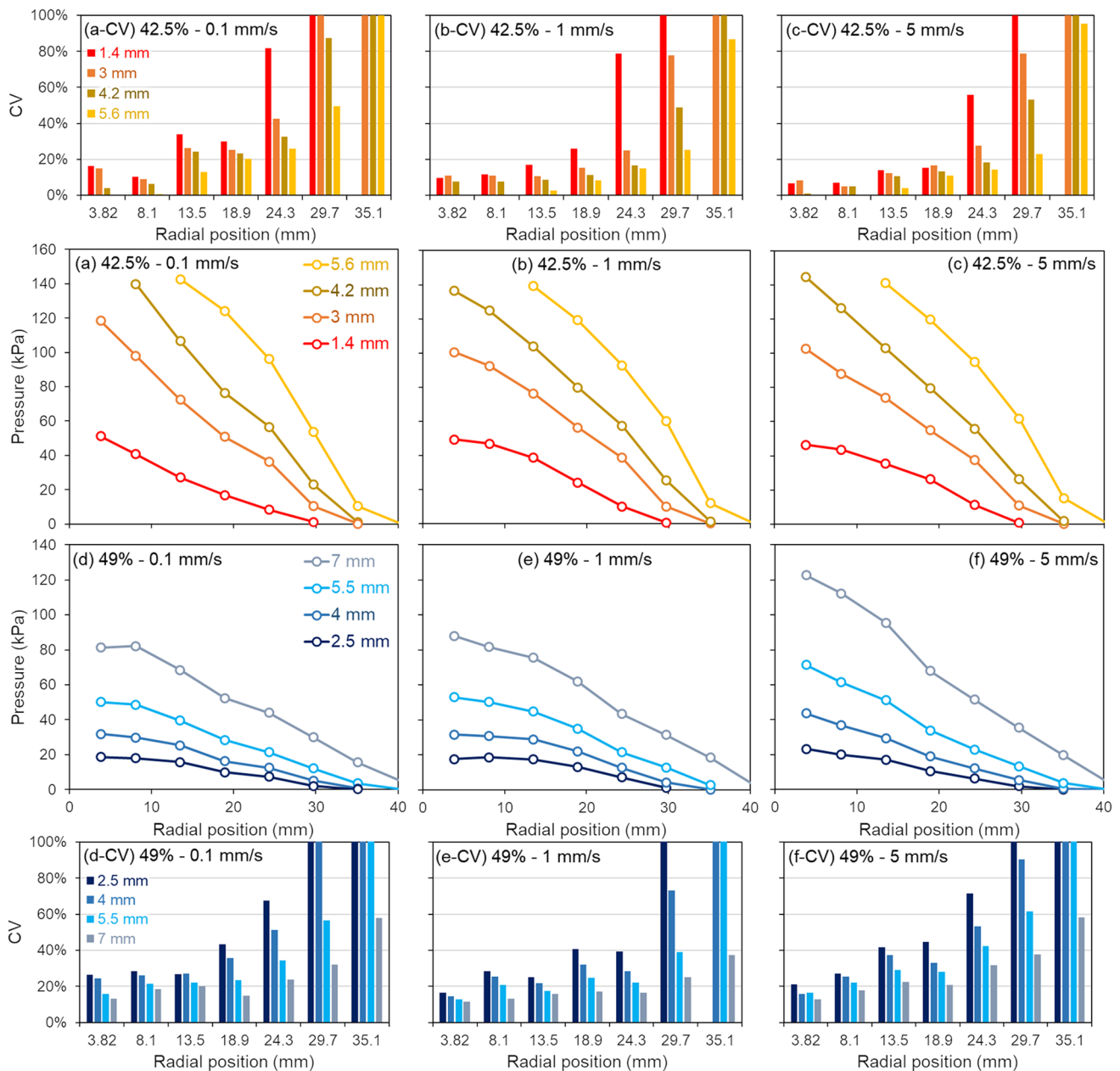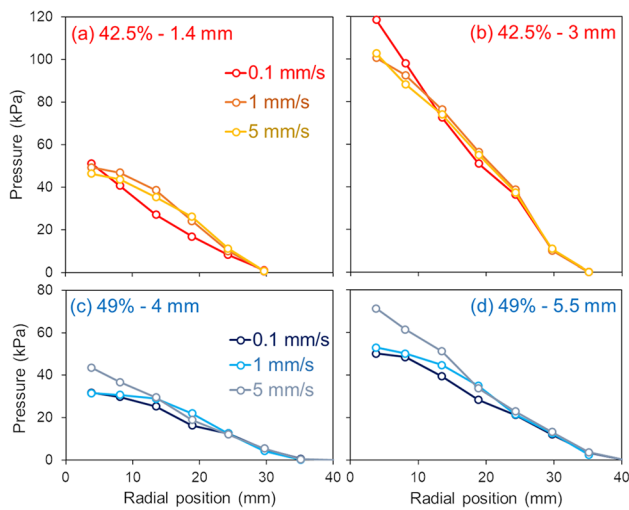
Fig. 15 Pressure distribution evolution for the tests with the clay with (**a**)-(**c**) 42.5% and (**d**)-(**f**) 49% of water content; (a-CV)-(f-CV) coefficient of variation for each data point represented

of slightly more homogeneous flow since the values of pressure along the circumferences are relatively closer. For the clay with 49% water content, the mean profile at 5 mm/s (Fig. 15f) starts to get higher values of pressure towards the end of the test in comparison with the tests at lower velocities with the same clay (Fig. 15d and Fig. 15e). This behavior also comes accompanied by slightly higher coefficient of variation at 5.5 mm and 7 mm of displacement (Fig. 15f-CV) than its counterparts (Fig. 15d-CV and Fig. 15e-CV).

To better highlight some of the slight differences commented above, even if the bulk squeeze force and general

outlines were quite similar for each water content, the same results can also be shown grouped by similar moments in tests with different displacement rates (Fig. 16). The squeeze flow of suspensions commonly shows a dependency of the testing speed (Collomb et al. 2004; Cardoso et al. 2009; Grandes et al. 2018), with an increase of the bulk force with higher displacement rates when viscous forces are dominant (Kotsikos and Gibson 1998; Mascia and Wilson 2008), and the opposite effect when phase separation takes place, since the percolation is favored by lower velocities, leading to more intense liquid phase migration and resulting frictional forces

Fig. 16 Pressure distribution in selected displacements for tests in three different displacement rates with the plastic clay with (**a**)-(**b**) 42.5% and (**c**)-(**d**) 49% of water content

between solid particles (Roussel and Lanos 2004; Grandes et al. 2021).

For the clay with 42.5% of water content, the tests at 1 mm/s and 5 mm/s had indeed very similar pressure distribution profiles. The test at 0.1 mm/s on the other hand showed a less parabolic and more exponential profile since early displacements (Fig. 16a), and higher pressure at the center of the sample in comparison with the other displacement rates later in the test (Fig. 16b). As seen in previous works, this can be an indication of phase separation effects, albeit still not intense enough to disturb the bulk response. For the clay with higher water content, however, the higher displacement rate was the one that presented a slight difference of behavior, with higher pressure in the central region, already noticeable at 4 mm (Fig. 16c) and more pronounced at 5.5 mm of displacement (Fig. 16d). As explained, this is an indication of a predominantly viscous response.

The differences observed, however, were very subtle and could easily be overlooked in an analysis based solely on the squeeze force curves. The material analyzed is a plastic clay, which is expected to present perfect plastic deformation and thus consistent behavior independently of the testing speed (Roussel and Lanos 2003). Even though the bulk behavior was very similar, the pressure mapping device allowed for a closer look into details that would go unseen, showing slight differences and providing richer information about the flow behavior of the material.

Comparison to theoretical models

Multiple models try to describe the force and pressure distribution for materials undergoing squeeze flow at different types of flow regime, and each of them involve certain boundary conditions and specific gradients for pressure profiles (Engmann et al. 2005; Muravleva 2015). The incorporation of pressure mapping provides detailed data about the actual pressure distribution and its evolution during the squeeze flow tests, which enables a direct comparison between existing models and experimental results (Grandes et al. 2018, 2021, 2023). This additional information facilitates the employment of theoretical models, serving as an indicator to flow types and other relevant factors.

This section compares the experimental pressure distributions obtained with predictions from models for Newtonian material under shear flow, biaxial extension, and perfect plastic deformation. It is important to highlight that the purpose is not exactly to fit the experimental results into the models, but instead to use theoretical profiles for different fluid behaviors as references for the dynamics and modifications that happen during the squeeze flow of the tested materials. For this purpose, the models listed were chosen as examples to demonstrate the potential of the method and illustrate the possibilities of analyses, also because these are models for pure and well-defined behaviors, with less parameters to be determined. Other models could also be interesting for comparison with these materials, but even more complex models show little variation in the curvature of the pressure profiles when the rheological parameters change (Muravleva 2017, 2019). At the current stage, this methodology is still not at the point of detail to make inferences with that level of precision. Moreover, it has been shown that even if simpler, Newtonian models may be appropriate as a first approximation to many types of flows even if the material presents yield stress (Zwick et al. 1996), especially for the constant speed squeeze flow case, since the flow will be induced regardless due the imposed displacement (Campanella and Peleg 1987; Steffe 1996).

Theoretical background and definition of parameters

A brief explanation including the main equations for the models employed is presented below, and their mathematical development is further detailed in previous works (Grandes et al. 2018, 2021). All the models require the information of the sample radius (R). Since for constant volume squeeze flow the area of the sample changes during the tests, R was determined for each moment according to the corrected radius value approach suggested in previous work with the same test setup (Grandes et al. 2021). The theoretical area from the constant volume hypothesis is used for the initial placing phase (to compensate for the areas where the pressure is still too low for the sensor to detect) and the radius calculated from the sensor contact area measurement is used for the rest of the test. As seen in

the "Sensor contact area vs. theoretical area" section, the sensor area and theoretical area are very similar throughout the tests analyzed in this paper. This might not be the case for other materials, so the approach using the area data provided by the pressure mapping system is considered more adequate for the model calculations.

For pure biaxial extension, the pressure is evenly distributed over the contact area; thus, there is no radial variation and the resulting distribution is flat (Kotsikos and Gibson 1998). In this case, the pressure (P_{biaxext}) can be calculated simply by dividing the total force by the sample area, as indicated by Eq. 3 where F is the compression force measured by the universal testing machine.

$$P_{\mathrm{biaxext}} = \frac{F}{\pi R^2} \tag{3}$$

From the boundary conditions of a general fluid under no-slip constant speed squeeze flow (Bird et al. 2002) and the compression force for a power law fluid under the same regime (Winther et al. 1991) taken for the simpler case of a Newtonian fluid (making the power law parameter n equal to one), the pressure for a Newtonian fluid under shear squeeze flow (P_{shear}) can be determined for each radial position r by Eq. 4.

$$P_{\mathrm{shear}}(r) = \frac{2F_{\mathrm{shear}}}{\pi R^4}\left(R^2 - r^2\right) \tag{4}$$

Finally, the model employed for perfect plastic deformation (Roussel and Lanos 2003) assumes that the stress field during flow is determined by a plastic yield value (K_i), which can be determined graphically using its relation to a reduced force parameter (F^*), as indicated by Eq. 5, where h is the sample height at each moment of the test.

$$F^* = \frac{Fh}{\pi R^3} = \frac{2K_i}{\sqrt{3}} * \frac{h}{R} + \frac{2K_i}{3} \tag{5}$$

Then, with the value of K_i, the pressure distribution according to the perfect plastic model for a no-slip condition (P_{plastic}) can be determined by Eq. 6.

$$P_{\mathrm{plastic}}(r) = \frac{2K_i}{h}(R - r) \tag{6}$$

Figure 17 presents the determination of the plastic yield value for the perfect plastic deformation model. Even though the overall results are not necessarily consistent with the perfect plastic hypotheses, some parts of the curves were close to the expected behavior, allowing the determination of K_i values indicated in the graphics. One of the assumptions of the model is that K_i does not change with the displacement rate; however for the clay with higher water content (Fig. 17b), the curves stabilized in different levels; thus, a distinct value of K_i was adopted
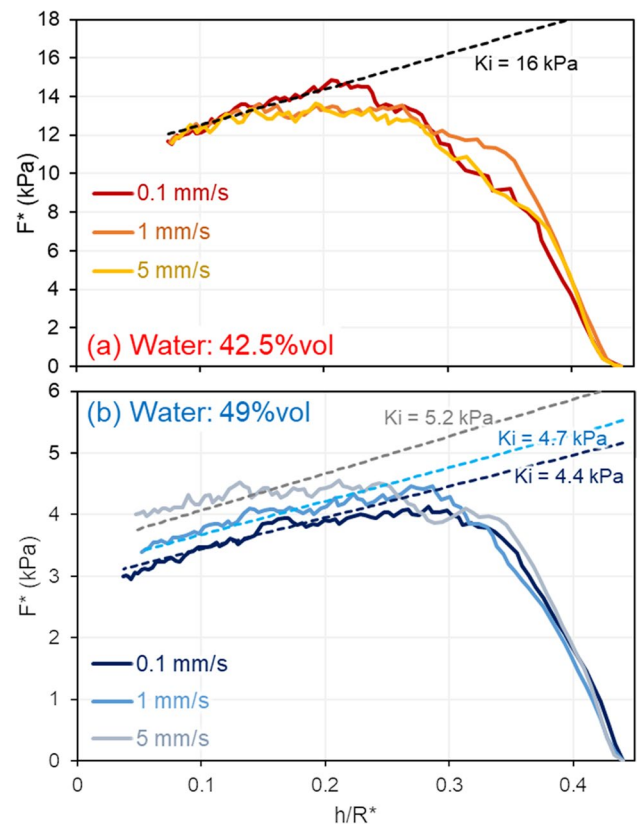

Fig. 17 Graphic determination of the perfect plastic model parameter (K_i) for the clay with (**a**) 42.5% and (**b**) 49% of water content

for each test. The values obtained for K_i for the clay with 49% water content — around 5 kPa — are consistent and indicate lower plasticity than what was observed for the lower water content. With more water available, the average distance between the solid particles increases, leading to more mobility and less overall cohesion for the suspension.

Equation 5 assumes no slip between the sample and the plate, and perfect shearing of the material. If there is slippage, the second term of the equation includes a different yield value (K_f instead of K_i), related to the lower friction leading to slip before the internal shearing can occur (Roussel and Lanos 2003), as indicated by Eq. 7.

$$F^*{}_{\mathrm{slip}} = \frac{2K_i}{\sqrt{3}} * \frac{h}{R} + \frac{2K_f}{3} \tag{7}$$

For most of the results presented in this work, however, better fits could not be determined considering values for K_f lower than K_i (more details presented in the Appendix); thus, only the no-slip perfect plastic deformation case was considered in the discussions. This also goes in line with other indications that the flow during the tests was closer to shear than elongational, including visual evidence of the

barreling effect, presented for identical interfacial conditions on mortars in a previous work (Grandes et al. 2021), and the analysis presented ahead in the "Pressure distribution: mean profile analysis" section.

Pressure distribution: mean profile analysis

The mean profile analysis is presented in Fig. 18, with the mean pressure and standard deviation calculated for each radial position as explained in the "Sensor data calibration and treatment" section. The graphics also include theoretical profiles for Newtonian shear flow, biaxial extension, and perfect plastic deformation models. Four displacements were selected for each test, in all three displacement rates for the plastic clay samples with 42.5% and 49% of water content.

A first general observation that can be made is that, in comparison with what was seen in this same type of analysis for cement mortars in previous works (Grandes et al. 2018, 2021, 2023), the pressure profiles are generally more regular and constant throughout the tests, and the error bars representing the standard deviation for each data point are much less intense, clear evidences of a more homogeneous flow as discussed in the previous sessions. This was also represented in Fig. 15, with the bar graphics indicating coefficient of variation values generally under 30% (excluding regions too close to the sample borders). In the pioneer work with the same combination of techniques, even for Newtonian materials the minimal standard deviation observed ranged from 20 to 50% of the mean pressure in each radial position (Yates 2003). Those values were even higher than the levels observed in this work, which can be attributed to differences of equipment and relative pressure levels, since pressures closer to the lower detection limit of the sensor tend to lead to higher variability.

Most of the experimental pressure profiles shown in Fig. 18 are close to the parabolic Newtonian shear curve or to the linear perfect plastic prediction. Even though the material analyzed is certainly non-Newtonian, the comparison to that simpler model has been proven adequate and useful for an indication of shear-type flow in previous works (Grandes et al. 2018). Even at moments that had points omitted due to saturation of the sensor (Fig. 18d,h,l) and thus relatively elevated pressure in the central region of the sample, the parts of the curve that were valid for representation were still quite close to the shear model predictions.

None of the experimental profiles resembles the biaxial extension model at all, with the only portion that gets close to the flat distribution being the central region of the 49% clay tested at 1 mm/s for early displacements (Fig. 18q). Other than that, the pressure at the borders of the samples tends to zero throughout all of the tests. Comparing to other results and theory from the literature, there is a clear difference of the pressure distribution from materials and conditions with higher influence of elongation (Kotsikos and Gibson 1998). Looking at fundamental models for elasto-plastic materials under different boundary conditions (Adams et al. 1991), the results also suggest low influence of an uniaxial yield stress value, since the pressure at the borders tends to non-significant values.

The setup and data processing employed here were able to demonstrate some important aspects of the flow. For an analysis more focused in exploring specific phenomena or details, it is also possible to make small improvements, adjustments, or modifications to the experimental procedure, providing even more precise information. For example, higher resolution of the sensor grid could provide more details about the edges of the sample and variations along the area. Dedicated tests with higher sensitivity of the sensor to increase detection of lower pressures would improve the data at the start of the tests and at the borders, facilitating the evaluation of yield stress and slip condition. These alternatives would allow for more precise inferences, and also the employment of more sophisticated and complex models, that require a higher level of detail (Muravleva 2019). Due to the number of variables and possibilities, all these cases should be analyzed in future works, also including materials with multiple types of behavior and different interfacial conditions, among other factors.

Error analysis

To quantify the proximity between experimental results and model predictions, an error analysis is proposed based on a coefficient of variation of the root-mean-squared error parameter, or CV(RMSE), which is the equivalent of a standard deviation between the experimental and calculated value (for each model separately) divided by the mean pressure to standardize the magnitude and allow comparison between different moments of the tests. CV(RMSE) is calculated for each displacement and model according to Eq. 8, where i corresponds to the identification of each circumference in the mean profile analysis (as explained in the "Sensor data calibration and treatment" section); $\overline{p}_i$ is the mean pressure in the i radial position; $\widehat{p}_i$ is the pressure estimated by the model being analyzes in the i radial position; n is the number of non-null values in the data set; and P is the mean pressure for the whole sample area in that moment of the test. The value of P coincides with the calculated value for the biaxial extension model (also presented in each graphic of Fig. 18), since for that behavior the pressure is constant along the whole area, and numerically that means the bulk force divided by the sample area.
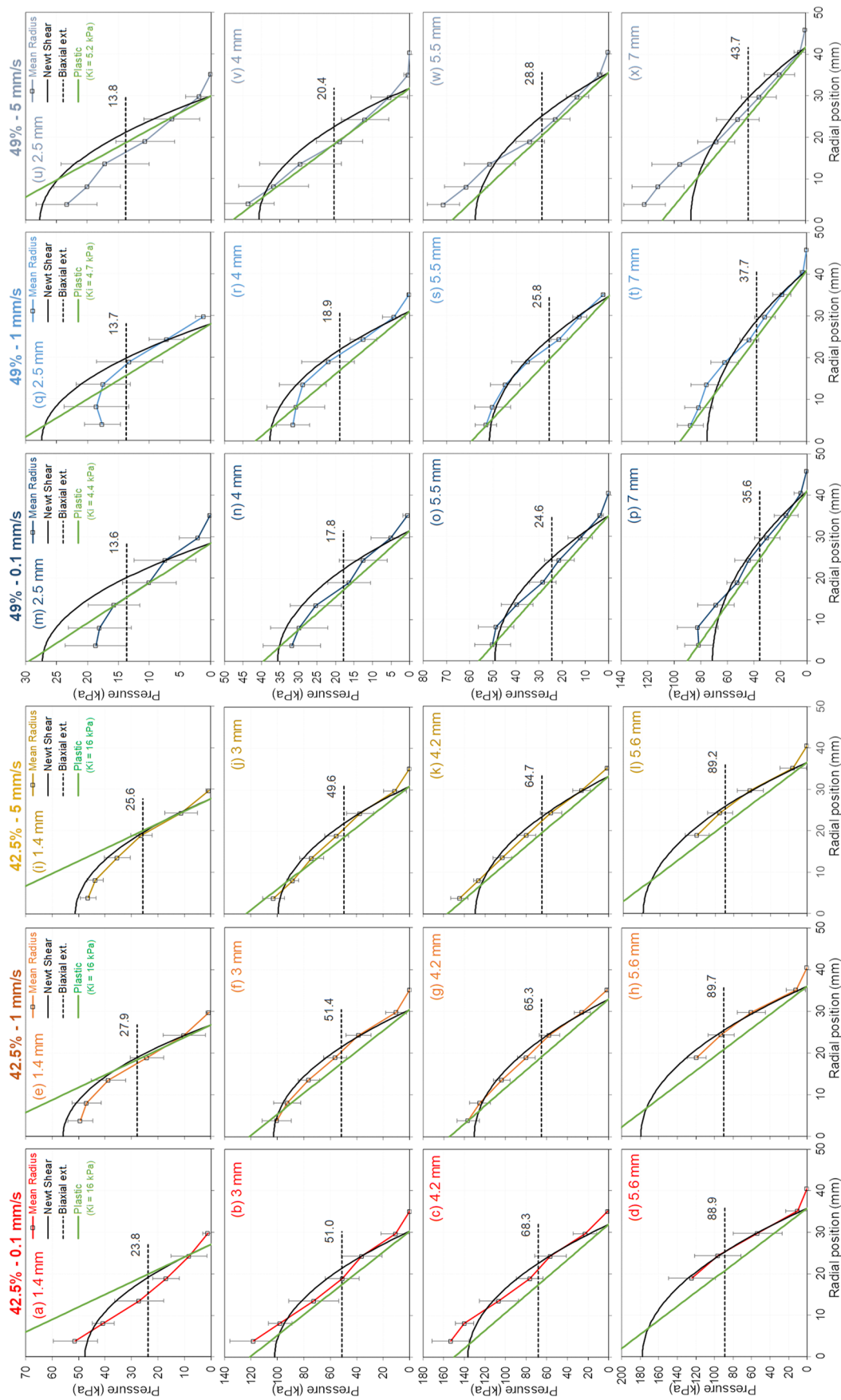
Fig. 18 Mean profile analysis of the squeeze flow tests with the plastic clay with (**a**)-(**l**) 42.5% and (**m**)-(**x**) 49% of water, in each of the three displacement rates employed; the sequence of displacements for each test is shown from top to bottom

$$CV(RMSE) = \frac{\sqrt{\frac{\sum_{i=1}^{n}(\bar{p}_i - \hat{p}_i)^2}{n}}}{P} \qquad (8)$$

The calculated values of CV(RMSE) for all tests are presented in Fig. 19, both for the Newtonian shear and plastic models. One first observation for the tests with lower water content (Fig. 19a,b,c) is that the CV(RMSE) values for the plastic models are relatively high for early displacements (up to around 2.5 mm). This happens because the model determines the pressure based solely on K_i, which does not take into account the first stage of the squeeze flow test. This is considered a placing phase and not covered by the model (Roussel and Lanos 2003; Toutou et al. 2005). For that reason, the experimental pressure is considerably lower than the pressure calculated through the model until the test reaches the second stage of plastic (or viscous) deformation. For the tests with higher water content (Fig. 19d,e,f), on the other hand, the error calculated for lower displacements is relatively high for both models. At 3 mm of displacement for these three tests, there are only a few sensing elements activated at the border of the samples that registered a raw value under 10 (in the raw scale of the sensor that ranges from 1 to 255), while most of the sample area displays higher pressures. Before that, the number of sensing elements with single digit raw values registered is more relevant. This means that the pressures at those early stages were too close to the lower measurement limit of the sensor setup employed, leading to not enough precision and resolution of pressure to adequately compare profiles to the predictions from the models. This is not as concerning for the clay with 42.5%, since the same pressure levels are reached much earlier (before 1 mm of displacement) for those tests.

After those initial moments, the comparisons in Fig. 19a,b,c seem to indicate that for the clay with 42.5% of water the experimental pressure distribution was generally closer to the shear model (CV(RMSE) around or under 10%) than to the plastic model predictions (CV(RMSE) around 20%) for all three displacement rates tested. For the clay with 49%, the comparison is not as distinct, with very similar values of error between both models, slightly lower for the shear model for part of the test at 1 mm/s (Fig. 19e), and slightly lower for the plastic model for part of the test at 5 mm/s (Fig. 19f). The proximity with the plastic model for the higher displacement rate can be related to the more viscous response obtained, increasing the pressure at the center of the sample as discussed in the "Pressure distribution: mean profile analysis" section and leading the profile closer to the linear plastic distribution. With lower test speed, there is more time for different kinetic effects to take place, such as elastic response and stress relaxation.
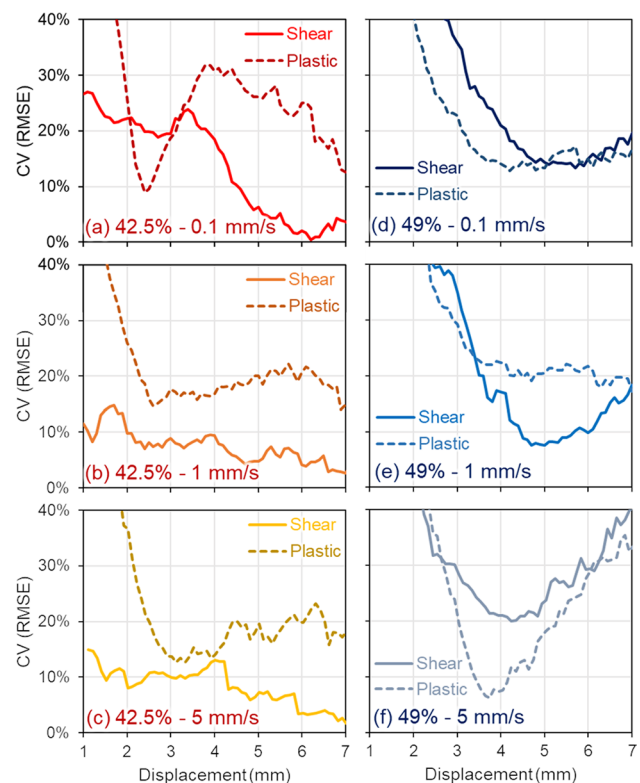
Fig. 19 CV(RMSE) analysis for all six tests performed comparing experimental mean profile results with the shear model and perfect plastic model predictions for the tests at 0.1, 1.0, and 5.0 mms with the clay with (a, b, c) 42.5% and (d, e, f) 49% water content

Variation of pressure along circumferences

Figure 20 presents the pressure distribution along the perimeter of three circumferences (R3, R4, and R5 as detailed in the "Sensor data calibration and treatment" section) at 3 mm of displacement for the tests with the clay with 42.5% of water at 0.1 mm/s (Fig. 20a) and 5 mm/s (Fig. 20b). The data sets shown in these two graphics lead to the values of mean pressure and standard deviation represented by the third, fourth, and fifth points from left to right in the mean profile curves shown in Fig. 18b and Fig. 18j, respectively. Other than the experimental values, the predicted pressure from the shear model for each radial position is also represented in the graphics, and standardized pressure curves (experimental pressure divided by the shear model values) are shown in Fig. 20c and Fig. 20d. This representation highlights the variation of the pressure around different angular positions in fixed radii over the sample area, which depending on the flow homogeneity over the sample area should display reasonably constant pressure due to the axisymmetric configuration.
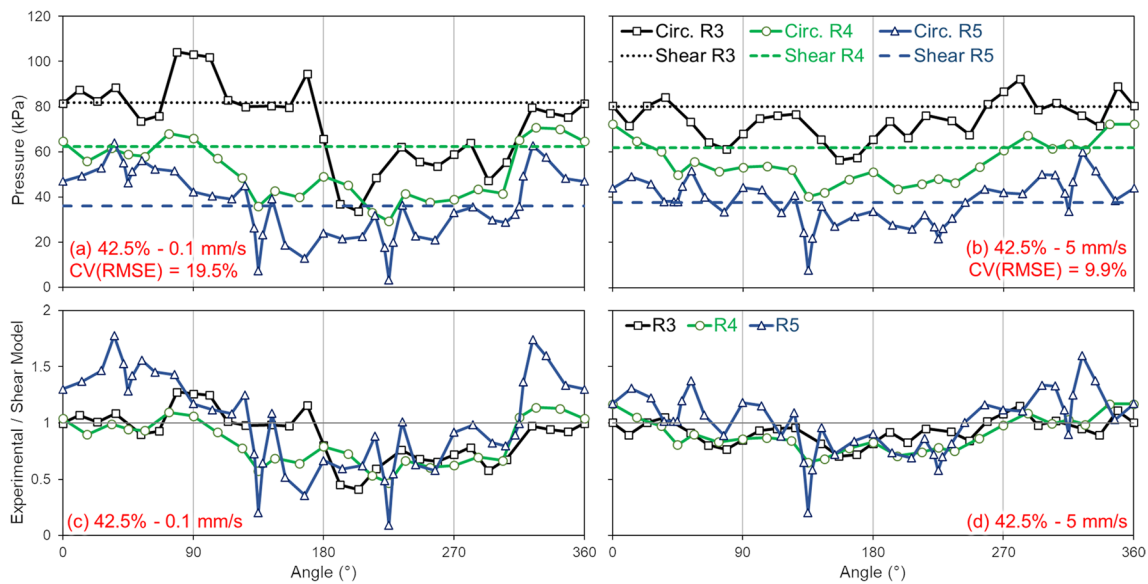
Fig. 20 Pressure distribution along circumferences R3, R4, and R5 at 3 mm of displacement for the tests with the 42.5% water content clay at **a** 0.1 mm/s and **b** 3.0 mm/s; ratio between experimental results and shear model predictions for **c** 0.1 mm/s and **d** 3.0 mm/s

Comparing both tests displayed, the difference in the variation firstly observed in the "Evolution of the pressure distribution" section becomes even clearer, as the range of pressures for each circumference is much wider for the test at 0.1 mm/s (Fig. 20a) in relation to the test at 5 mm/s (Fig. 20b). Even for the test at lower displacement rate, however, the variation is still lower than what has been reported for cement-based mortars in a similar representation (Grandes et al. 2023). The new standardized visualization of the results presented here for the first time in Fig. 20c and Fig. 20d makes it easier to compare results with different pressure levels, either from different displacements of a tests, different tests, or different radial positions from a single moment of a test.

The values of CV(RMSE) are also displayed within the graphics for reference. The parameter represents the difference between the mean experimental pressure and the model for each radial position; therefore, it is not the same as the variation depicted in these graphics even though both can be related in a certain level. The fluctuation of the pressure levels can still be low, yet around a mean pressure that is different from the model prediction. This is the case for some of the results presented, distinctively for example for R3 and R4 of the test at 5 mm/s (Fig. 20d), for which most of the data points display lower values than the shear model baseline.

Conclusions

This paper presented pressure mapped squeeze flow in its state of the art, with a detailed step-by-step explanation of the experimental procedure, calibration, data treatment, and extensive types of analysis that can be performed comprising bulk stress results, contact area as measured by the sensor, evolution of the mean pressure profile, comparison with models, error analysis, and multiple alternatives of data representation to highlight different aspects of the flow. With this methodology, PMSF could be replicated in other works, allowing for more detailed information about different types of materials in confined flows under compression.

The technique provided a much more thorough analysis of the plastic clay in both levels of water content evaluated. In comparison, the higher heterogeneity of mortars analyzed in previous works led to bigger variations that were easier to detect, but even the more homogeneous and continuous behavior of the plastic clay from this work had detailed aspects that were only revealed by the closer look of pressure mapping. Even though the bulk stress curves were very similar between the displacement rates for each set of tests with the same water content, the method was able to detect small divergencies in the mean pressure profiles. These findings suggest slight influence of the test speed and thus different intensity for the multiple phenomena that take place during squeeze flow.

After the comparison with theoretical models performed, supported by the error analysis proposed, none of the models employed can fully explain the flow that occurs during the tests. Nonetheless, the detailing presented offers a direct and quick indication to which type of modelled behaviors is closer to the measured pressure distributions in each moment of the tests. Even though the material is technically plastic, the profiles were closer to the shear model than to the perfect plastic for most parts of the tests with lower water content, and somewhat in between both models throughout the tests with the clay with higher water content. The determination of the yield parameter for the plastic model pointed to different values for each displacement rate with the lower water content clay, which already suggests that the perfect plastic behavior was not achieved. The combination of the analysis from the evolution of the pressure profiles and the attempts to determine parameters for the plastic model all indicate a flow in predominantly shear conditions.

This work demonstrates how the addition of pressure mapping enhances the already valuable squeeze flow test by providing new levels of information. Different types of flow can lead to very similar bulk responses when all the multiple factors are added up. The closer look provided by the improved technique can bring forward more details regarding the rheological nature and related phenomena, enriching the interpretation of the results and the understanding of the flow. PMSF is versatile and can still be improved even further. The method allows for choices of experimental setup and parameters to focus on certain aspects of interest depending also on material characteristics, expected type of behavior, and other factors. A denser grid

with more sensing elements within the sample area or a wider range to better cover the different pressure levels, or even dedicated tests with specific sensitivity setups for pressure levels of interest, could enhance data acquisition and facilitate analyses. This would lead to even further details and clearer information regarding the phenomena taking place, possibly enabling the employment of more complex models and more thorough inferences such as determining areas with different flow types, interfacial slip, or how much of a mixed behavior is happening within the sample.

Appendix

The perfect plastic deformation model employed (Roussel and Lanos 2003) suggests a variation for the case of slippage, as discussed in the "Theoretical background and definition of parameters" section. Figure 21 presents the attempt to fit the results into this hypothesis and determine both K_i and K_f through linear regression and according to Eq. 7.

From the linear regression, K_i is determined by the slope and K_f by the intercept. As observed, for most of the tests, the value obtained for K_f was higher than the one obtained for K_i (Fig. 21c,d,e,f), which goes against the logic of the model (K_f has to be lower than K_i; otherwise, no slip occurs and $K_f = K_i$, resulting in the case represented by Eq. 5) (Roussel and Lanos 2004). Moreover, the values of K_i also showed considerable variation for different displacement rates within each set with the same water content, which should not be the case since K_i is a yield
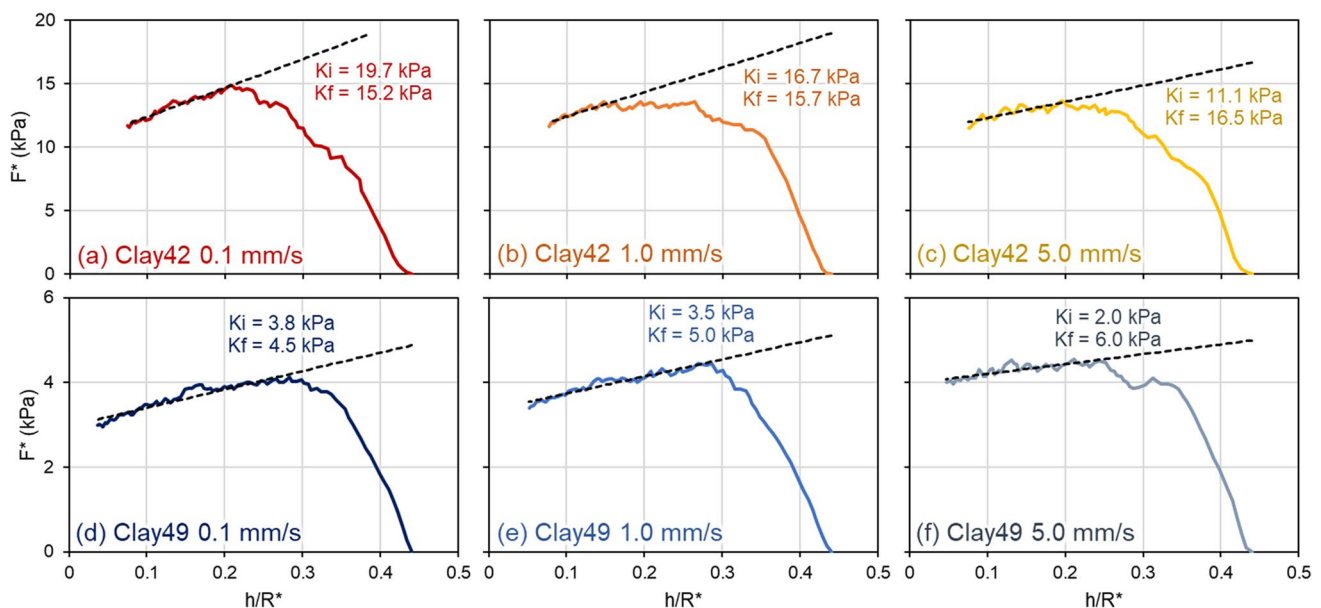
Fig. 21 Graphical determination of the yield values K_i and K_f for the perfect plastic model considering slippage, for the tests in all three displacement rates using the clay with (a, b, c) 42.5% and (d, e, f) 49% of water content

value for internal shearing of the material, not depending on the test condition (Roussel and Lanos 2003).

Since the determination of yield parameters led to the inconsistencies discussed above, it was considered that the model under these hypotheses does not represent well the behavior of the materials analyzed. This was also seen as another evidence that there was no significant slippage at the interfaces during the tests. Therefore, this variation of the model was not employed for the analysis and discussions in the present paper. This same evaluation, however, could be used more successfully for different tests with materials closer to the perfect plastic behavior and changing interfacial conditions to test the influence of slippage.

Data availability The datasets generated and analysed during the current study are available from the corresponding author on reasonable request.

Declarations

Competing interests The authors declare no competing interests.

References

Adams MJ, Aydin İ, Briscoe BJ, Sinha SK (1997) A finite element analysis of the squeeze flow of an elasto-viscoplastic paste material. J Non-Newton Fluid Mech 71:41–57. https://doi.org/10.1016/S0377-0257(96)01546-7

Adams MJ, Biswas SK, Briscoe BJ, Kamyab M (1991) The effects of interface constraints on the deformation of pastes. Powder Technol 65:381–392. https://doi.org/10.1016/0032-5910(91)80200-3

Adams MJ, Briscoe JB, Kamjab M (1993) The deformation and flow of highly concentrated dispersions. Adv Colloid Interface Sci 44:143–182. https://doi.org/10.1016/0001-8686(93)80023-5

Andrade FA, Al-Qureshi HA, Hotza D (2011) Measuring the plasticity of clays: a review. Appl Clay Sci 51:1–7. https://doi.org/10.1016/j.clay.2010.10.028

Bird RB, Stewart WE, Lightfoot EN (2002) Transport phenomena, Revised 2nd Edition, 2nd edn. Wiley

Campanella OH, Peleg M (1987) Squeezing flow viscosimetry of peanut butter. J Food Sci 52:180–184. https://doi.org/10.1111/j.1365-2621.1987.tb14000.x

Cardoso FA, John VM, Pileggi RG (2009) Rheological behavior of mortars under different squeezing rates. Cem Concr Res 39:748–753. https://doi.org/10.1016/j.cemconres.2009.05.014

Cardoso FA, John VM, Pileggi RG, Banfill PFG (2014) Characterisation of rendering mortars by squeeze-flow and rotational rheometry. Cem Concr Res 57:79–87. https://doi.org/10.1016/j.cemconres.2013.12.009

Chatraei Sh, Macosko CW, Winter HH (1981) Lubricated squeezing flow: a new biaxial extensional rheometer. J Rheol 25:433–443. https://doi.org/10.1122/1.549648

Collomb J, Chaari F, Chaouche M (2004) Squeeze flow of concentrated suspensions of spheres in Newtonian and shear-thinning fluids. J Rheol 48:405–416. https://doi.org/10.1122/1.1645514

Coussot P (2005) Rheometry of pastes, suspensions, and granular materials: applications in industry and environment. John Wiley & Sons

Denn MM, Marrucci G (1999) Squeeze flow between finite plates. J Non-Newton Fluid Mech 87:175–178. https://doi.org/10.1016/S0377-0257(99)00062-2

Engmann J, Servais C, Burbidge AS (2005) Squeeze flow theory and applications to rheometry: a review. J Non-Newton Fluid Mech 132:1–27. https://doi.org/10.1016/j.jnnfm.2005.08.007

Estellé P, Lanos C, Perrot A, Servais C (2006) Slipping zone location in squeeze flow. Rheol Acta 45:444–448. https://doi.org/10.1007/s00397-005-0070-2

Grandes FA, Rego ACA, Rebmann MS, et al (2023) Pressure mapped squeeze flow (PMSF): extending rheological characterization of mortars beyond traditional rheometry. Int J Ceram Eng Sci n/a:e10174 https://doi.org/10.1002/ces2.10174

Grandes FA, Sakano VK, Rego ACA et al (2018) Squeeze flow coupled with dynamic pressure mapping for the rheological evaluation of cement-based mortars. Cem Concr Compos 92:18–35. https://doi.org/10.1016/j.cemconcomp.2018.05.016

Grandes FA, Sakano VK, Rego ACA et al (2021) Rheological behavior and flow induced microstructural changes of cement-based mortars assessed by pressure mapped squeeze flow. Powder Technol 393:519–538. https://doi.org/10.1016/j.powtec.2021.07.082

Ino K, Cardoso FA, Valencia GA, et al (2020) Rheological evaluation of phosphatic porcelain using squeeze flow technique. Ceram Mod Technol 2 https://doi.org/10.29272/cmt.2019.0016

Kotsikos G, Bland JH, Gibson AG (1999) Rheological characterization of commercial glass mat thermoplastics (GMTs) by squeeze flow testing. Polym Compos 20:114–123. https://doi.org/10.1002/pc.10339

Kotsikos G, Bland JH, Gibson AG, Chandler HW (1996) Squeeze flow testing of glass mat thermoplastic material. Compos Part Appl Sci Manuf 27:1195–1200. https://doi.org/10.1016/1359-835X(96)00077-2

Kotsikos G, Gibson AG (1998) Investigation of the squeeze flow behaviour of sheet moulding compounds (SMC). Compos Part Appl Sci Manuf 29:1569–1577. https://doi.org/10.1016/S1359-835X(98)00094-3

Lipscomb GG, Denn MM (1984) Flow of Bingham fluids in complex geometries. J Non-Newton Fluid Mech 14:337–346. https://doi.org/10.1016/0377-0257(84)80052-X

Mascia S, Wilson DI (2008) Biaxial extensional rheology of granular suspensions: the HBP (Herschel-Bulkley for pastes) model. J Rheol 52:981–998. https://doi.org/10.1122/1.2930876

Meeten GH (2004) Effects of plate roughness in squeeze-flow rheometry. J Non-Newton Fluid Mech 124:51–60. https://doi.org/10.1016/j.jnnfm.2004.07.003

Min BH, Erwin L, Jennings HM (1994) Rheological behaviour of fresh cement paste as measured by squeeze flow. J Mater Sci 29:1374–1381. https://doi.org/10.1007/BF00975091

Muravleva L (2015) Squeeze plane flow of viscoplastic Bingham material. J Non-Newton Fluid Mech 220:148–161. https://doi.org/10.1016/j.jnnfm.2015.01.012

Muravleva L (2017) Axisymmetric squeeze flow of a viscoplastic Bingham medium. J Non-Newton Fluid Mech 249:97–120. https://doi.org/10.1016/j.jnnfm.2017.09.006

Muravleva L (2019) Axisymmetric squeeze flow of a Herschel-Bulkley medium. J Non-Newton Fluid Mech 271:104147. https://doi.org/10.1016/j.jnnfm.2019.104147

Nikkhoo M, Hofman A, Gadala-Maria F (2014) Radial filtration in highly concentrated suspensions undergoing constant-force squeeze flow and its effect on the normal stress distribution. Rheol Acta 53:303–314. https://doi.org/10.1007/s00397-014-0763-5

Nikkhoo M, Khodabandehlou K, Brozovsky L, Gadala-Maria F (2013) Normal stress distribution in highly concentrated suspensions undergoing squeeze flow. Rheol Acta 52:155–163. https://doi.org/10.1007/s00397-013-0681-y

Rabideau BD, Lanos C, Coussot P (2009) An investigation of squeeze flow as a viable technique for determining the yield stress. Rheol Acta 48:517–526. https://doi.org/10.1007/s00397-009-0347-y

Roussel N, Lanos C (2004) Particle fluid separation in shear flow of dense suspensions: experimental measurements on squeezed clay pastes. Appl Rheol 14:256–265. https://doi.org/10.1515/arh-2004-0015

Roussel N, Lanos C (2003) Plastic fluid flow parameters identification using a simple squeezing test. Appl Rheol 13:132–141. https://doi.org/10.1515/arh-2003-0009

Stading M (2021) Bolus rheology of texture-modified food: effect of degree of modification. J Texture Stud 52:540–551. https://doi.org/10.1111/jtxs.12598

Steffe JF (1996) Rheological methods in food process engineering. 2nd edn. Freeman Press, East Lansing

Törnqvist R, Sunderland P, Månson JAE (2000) Non-isothermal process rheology of thermoplastic composites for compression flow moulding. Compos Part Appl Sci Manuf 31:917–927. https://doi.org/10.1016/S1359-835X(00)00048-8

Toutou Z, Roussel N, Lanos C (2005) The squeezing test: a tool to identify firm cement-based material's rheological behaviour and evaluate their extrusion ability. Cem Concr Res 35:1891–1899. https://doi.org/10.1016/j.cemconres.2004.09.007

Winther G, Almdal K, Kramer O (1991) Determination of polymer melt viscosity by squeezing flow with constant plate velocity. J Non-Newton Fluid Mech 39:119–136. https://doi.org/10.1016/0377-0257(91)80009-9

Yates NM (2003) The squeeze flow rheometry of foods. PhD Thesis, University of Birmingham

Zwick KJ, Ayyaswamy PS, Cohen IM (1996) Variational analysis of the squeezing flow of a yield stress fluid. J Non-Newton Fluid Mech 63:179–199. https://doi.org/10.1016/0377-0257(95)01423-3